Supporting Information

Cu^{2+}-Activated NIR Photothermal Conversion Based on Imine Bond Photorotation for Dual-Mode Antibacterial Applications

Weiqi Yu[1], Hao Qiu[1], Menghui Lin[1], Xiaolong Zhang[1], Shunwei Chen[1*], Zifei Wang[1], Mingzhi Wei[1], Conghui Si[1], Xiujun Han[1*], and Xujun Zheng[2*]

[1]Shandong Key Laboratory of Advanced Glass Manufacturing and Technology, School of Materials Science and Engineering, Qilu University of Technology (Shandong Academy of Sciences), Jinan 250353, China

[2]Department of Materials Science and Engineering, University of Virginia, Charlottesville, VA 22904, USA

Contents

Equipment

The nuclear magnetic resonance (NMR) spectra were recorded at 25°C on a 400 MHz spectrometer (JEOL JNM-ECZL400S). The Fourier transform infrared spectroscopy (FTIR) spectrum was measured by Shimadzu IR Prestige-21 spectrometer. The single crystal X-ray diffraction (XRD) analysis was conducted by Bruker D8 Quest using Cu Kα radiation. The absorption spectra were acquired on the Shimadzu UV-3600Plus spectrophotometer, and the photoluminescence spectra were obtained on a steady-state and time-resolved photoluminescence spectrometer (Edinburgh FLS1000). The 660 and 808 nm lasers are used as light sources (VCL-660nm and VCL-808nm, Blueprint). The temperature changes induced by photothermal effects were recorded using an infrared thermal imager (Hikvision H13Pro). The bacterial photoluminescence imaging was performed using Nikon ECLIPSE Ti2 as the confocal laser scanning microscope (CLSM). The scanning electron microscopy (SEM) analysis was conducted with ZEISS GeminiSEM 500.

Calculation of photothermal conversion efficiency

The photothermal conversion efficiency (PTCE) was calculated according to the reported method[1]. Under continuous laser irradiation (808 nm or 660 nm), the temperatures of photothermal agents in solution were recorded. The photothermal conversion efficiency (PTCE) was then calculated according to Equation (1):

$$\eta = \frac{hs\left(T_{max} - T_{surr}\right) - Q_0}{I\left(1 - 10^{-A_\lambda}\right)} \#\ (1)$$

where h is the heat transfer coefficient, s is the surface area of the container, T_{max} is the maximum temperature of the solution in the cuvette, and T_{surr} is the ambient temperature. Q_0 represents the heat loss, I is the laser intensity ($W \cdot cm^{-2}$), and A_λ denotes the absorbance of the solution at 660 or 808 nm.

$$Q_0 = hs\left(T_{max}^{'} - T_{surr}\right) \#\ (2)$$

where T'_{max} denotes the maximum temperature of the solvent. hs can be calculated using Equation (3):

$$hs = \frac{mC_{solvent}}{\tau_s} \#\ (3)$$

where *m* denotes the mass of the solution (g), $C_{solvent}$ represents the heat capacity of ethanol (2.42 J/g), and τ_s is the time constant of the system, which can be calculated using Equation (4):

$$\tau_s = \frac{t}{-\ln \Theta} \#\ (4)$$

where *t* is the time of the cooling process, and ϑ is a dimensionless parameter of which the value can be obtained from Equation (5):

$$\Theta = \frac{T - T_{surr}}{T_{max} - T_{surr}} \#\ (5)$$

where *T* represents the real-time temperature during the cooling period.

Job's plot measurement

The coordination ratio of BTAA-Et with Cu^{2+} was determined by a Job's plot method, in which a constant total molar concentration (5 μM) was maintained while varying the component ratios of BTAA-Et and Cu^{2+}. The changes in light absorption intensity at 670 nm were measured for analysis.

Antibacterial measurements

A blank control was prepared by mixing 100 μL of a bacterial suspension (10^7 CFU·ml^{-1}) with 900 μL of PBS buffer. For the experimental groups, 100 μL of bacterial suspension was added to 900 μL of ultrapure water containing BTAA-Et (200 μmol), Cu^{2+} (200 μmol), Cu^{2+}@BTAA-Et (100 μmol), or Cu^{2+}@BTAA-Et (200 μmol). After the 2-hour incubation, each mixture was immediately divided into three equal aliquots, which were then individually exposed to an 808 nm laser (0.60 W·cm^{-2}) for 0, 10, and 20 minutes, respectively. After irradiation, the samples were serially diluted, plated by spreading, and incubated for 12 hours prior to colony counting[2].

Bacterial staining assay

S. aureus and *E. coli* suspensions (10^8 CFU/mL) were centrifuged at 8000 rpm for 3 minutes and washed 3 times with PBS buffer. The bacterial pellets were then resuspended and incubated for one hour with PBS buffer (control), BTAA-Et (200

μmol), Cu^{2+} (200 μmol), or Cu^{2+}@BTAA-Et (100 and 200 μmol). The solution of fluorescent dye was prepared by dissolving 10 mg of ethidium bromide (EB) in 10 mL PBS. The bacterial suspensions were stained with EB solution and then incubated in the dark for 15 minutes. The samples were washed 3 times with PBS to remove unbound dye. Finally, the bacteria were imaged using the confocal laser scanning microscope[3, 4].

SEM test

The sample preparation for SEM analysis was conducted over a 3-day procedure. On Day 1, the bacterial suspension was centrifuged at 8000 rpm for 3 minutes. The pellet was washed 3 times with PBS buffer via successive centrifugation and resuspension. The washed pellet was then fixed overnight at 4°C using 2.5% glutaraldehyde. On Day 2, the fixative was removed, and the sample was rinsed with 0.1 M PBS buffer for 15 minutes and then centrifuged. This rinsing step is repeated 3 times. A series of ethanol solutions (30%, 50%, 70%, and 90% ethanol) was then used for dehydration. Each sample was incubated for 15 minutes before centrifugation, followed by two 20-minute treatments with absolute ethanol. The sample was incubated in a 1:1 mixture of ethanol and isoamyl acetate for 30 minutes, then stored in pure isoamyl acetate overnight at 4°C. On Day 3, the sample solution was mixed thoroughly, a drop of the suspension was pipetted onto a glass slide and allowed to dry, and the prepared samples were then analyzed[3].

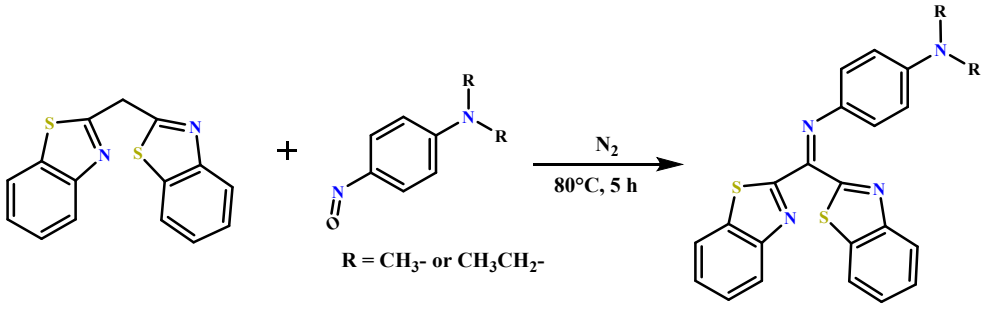

Scheme S1. Synthesis of BTAA-Me and BTAA-Et.

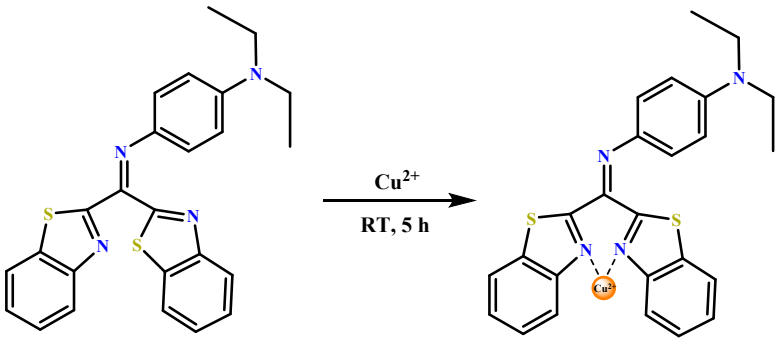

Scheme S2. Synthesis of the Cu^{2+}@BTAA-Et complex.

^{1}H NMR of BTAA-Me (400 MHz, DMSO-D_6): δ 8.24 (d, J = 7.9 Hz, 1H), 8.15 (dd, J = 8.5, 6.2 Hz, 2H), 7.98 – 7.92 (m, 1H), 7.65 – 7.55 (m, 2H), 7.53 – 7.48 (m, 2H), 6.89 (d, J = 9.0 Hz, 2H), 6.58 (d, J = 9.2 Hz, 2H), 2.89 (s, 6H).

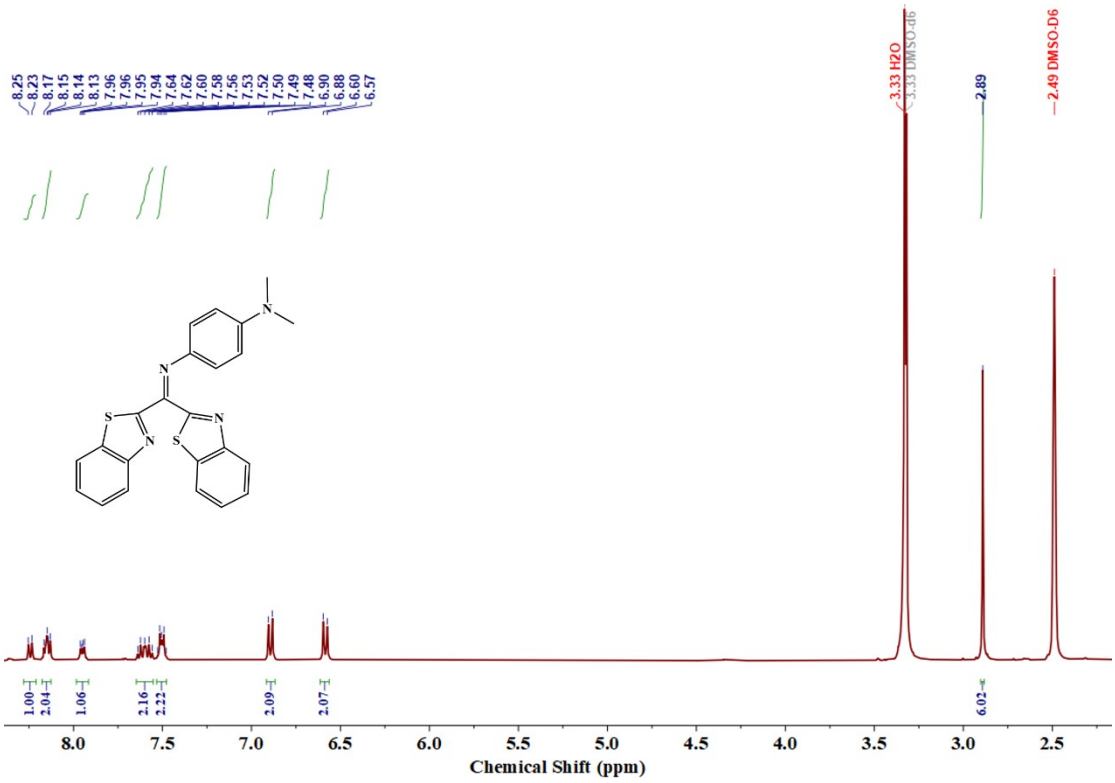

Figure S1. ^{1}H NMR spectrum of BTAA-Me.

^{1}H NMR spectrum of BTAA-Et (400 MHz, DMSO-D_6): δ 8.27 (d, J = 7.7 Hz, 1H), 8.19 – 8.12 (m, 2H), 7.94 (dd, J = 6.4, 3.0 Hz, 1H), 7.67 – 7.56 (m, 2H), 7.53 – 7.47 (m, 2H), 6.88 (d, J = 9.2 Hz, 2H), 6.55 (d, J = 9.3 Hz, 2H), 3.31 (q, J = 7.0 Hz, 4H), 1.03 (t, J = 6.9 Hz, 6H).

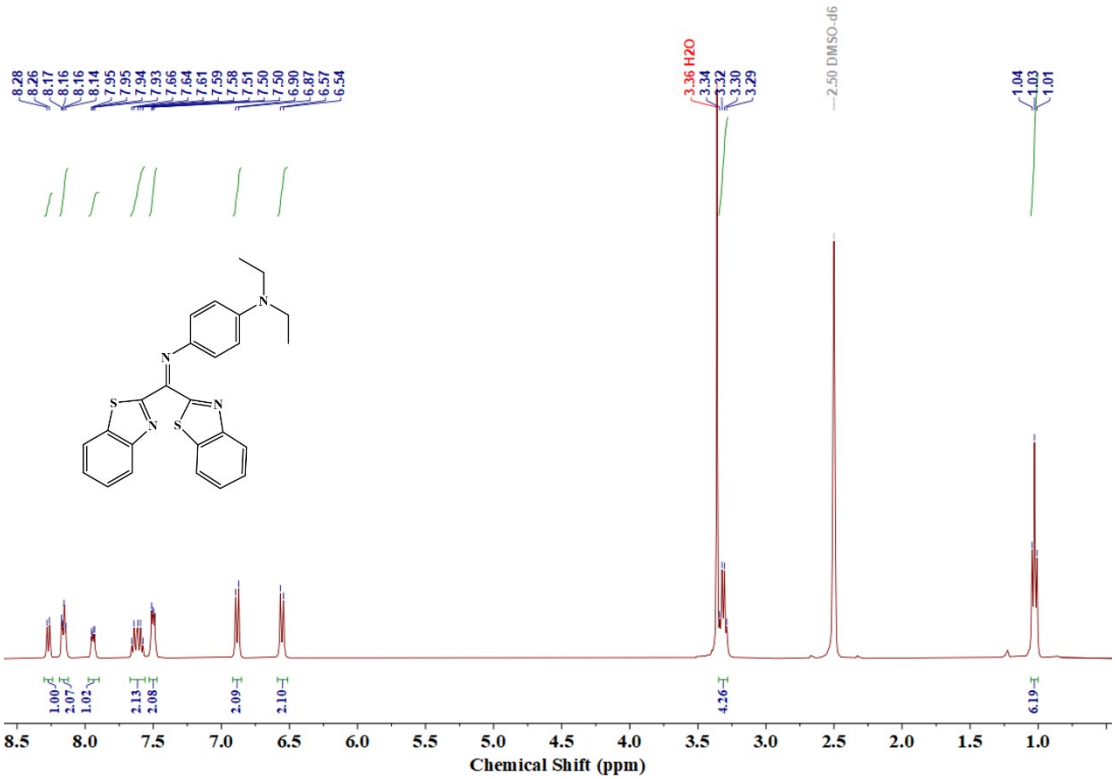

Figure S2. ^{1}H NMR spectrum of BTAA-Et.

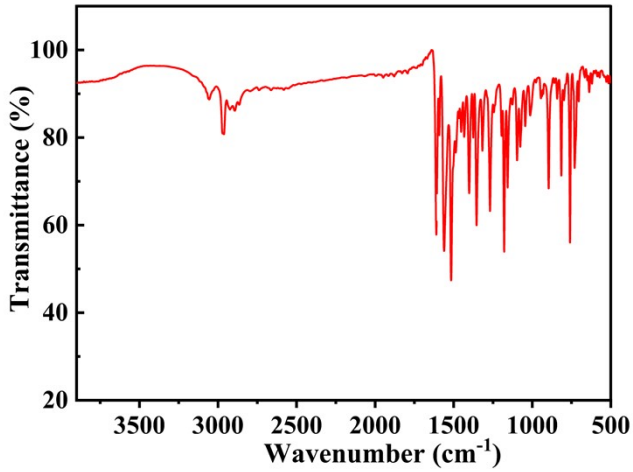

Figure S3. FTIR spectrum of BTAA-Et.

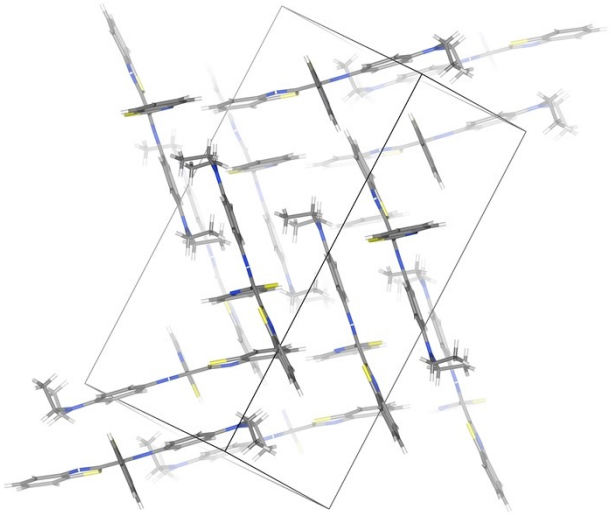

Figure S4. Molecular packing in BTAA-Et crystals.

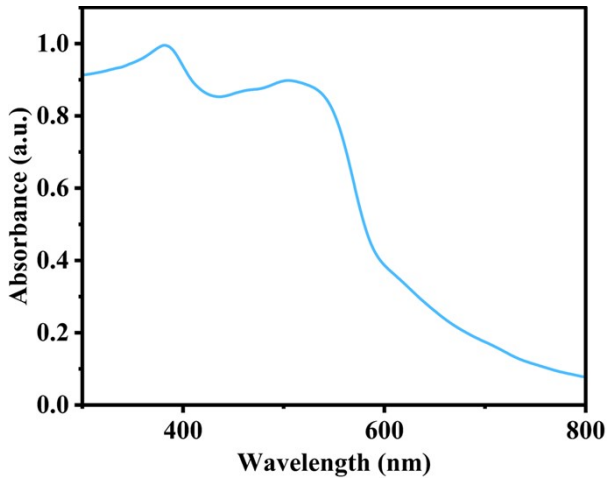

Figure S5. Normalized UV-Vis-NIR absorption spectrum of BTAA-Me in the solid state.

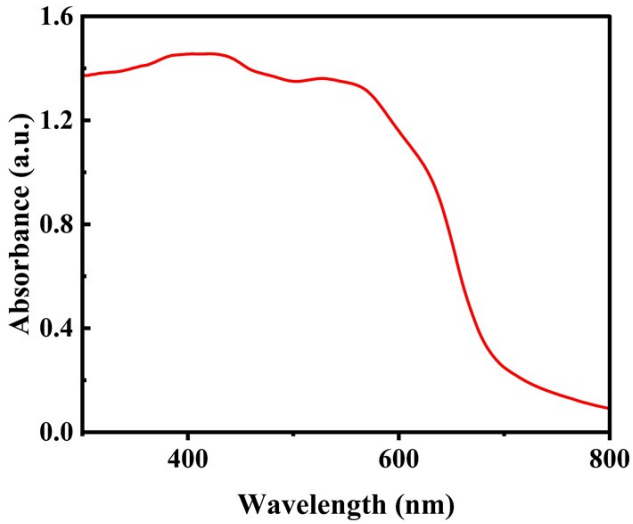

Figure S6. Normalized UV-Vis-NIR absorption spectrum of BTAA-Et in the solid state.

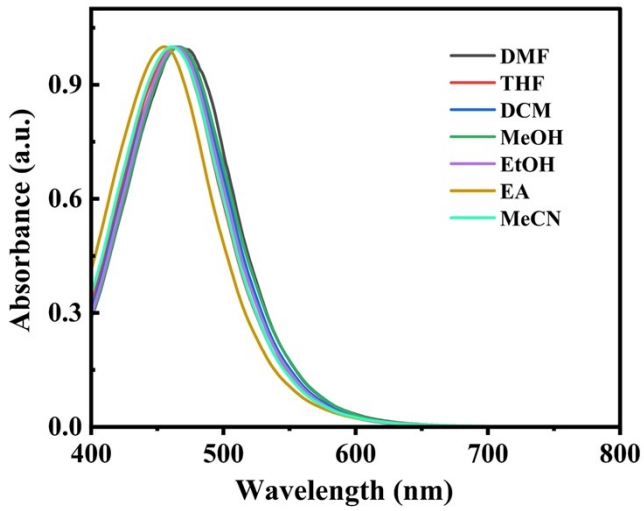

Figure S7. Normalized absorption spectra of BTAA-Me in solutions with varying polarity.

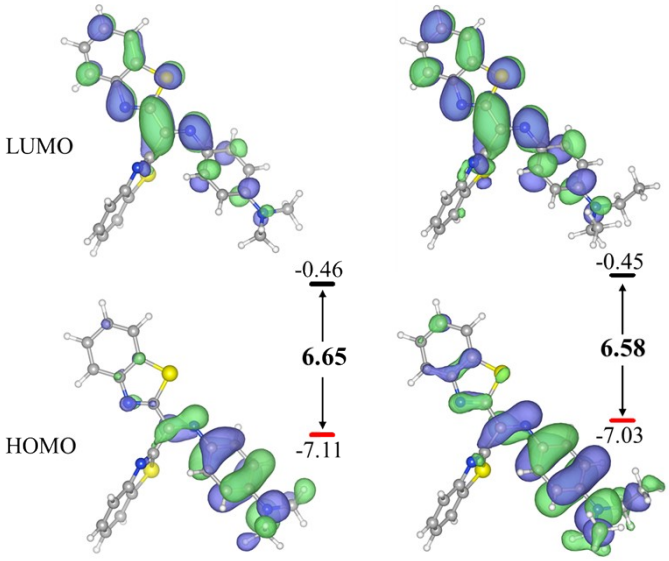

Figure S8. Distributions and energy levels of the highest occupied molecular orbital (HOMO) and lowest unoccupied molecular orbital (LUMO) of BTAA-Me and BTAA-Et (energy unit in eV).

Table S1. Excitation energy, oscillator strength (*f*), and main contributing molecular orbitals for first electronic transition ($S_0 \rightarrow S_1$).

Molecule	Excitation energy (eV)	*f* (a.u.)	Dominant contribution
BTAA-Me	3.347	0.555	HOMO→LUMO 80.3%
BTAA-Et	3.317	0.630	HOMO→LUMO 81.4%

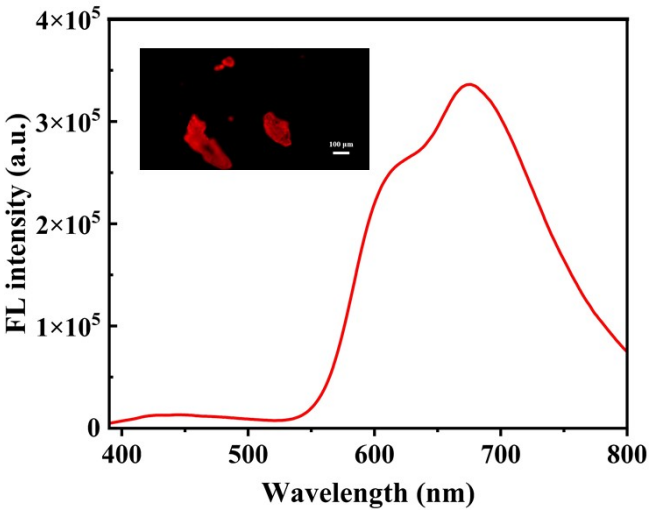

Figure S9. Photoluminescence spectrum and CLSM image of BTAA-Et.

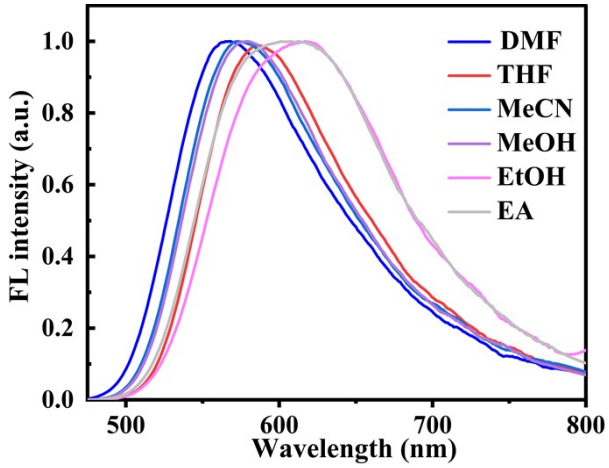

Figure S10. Photoluminescence spectra of BTAA-Et in solutions with varying polarity.

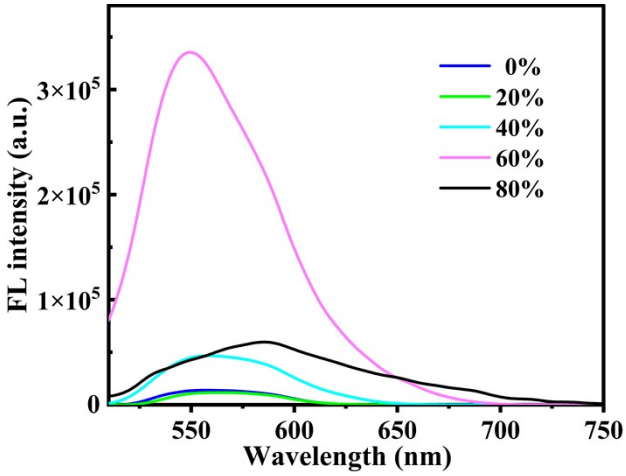

Figure S11. H_2O volume ratio-dependent photoluminescence of BTAA-Et in THF.

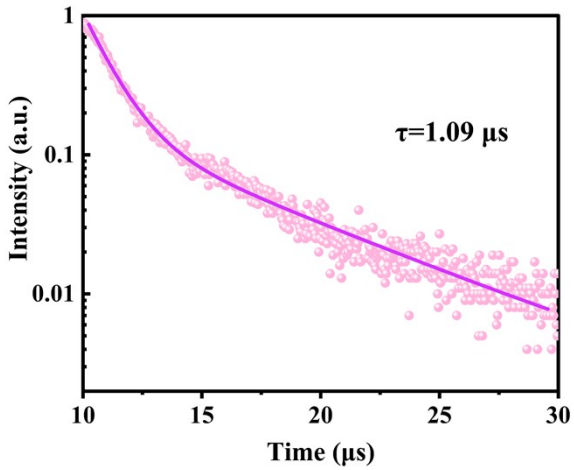

Figure S12. Transient PL decay curve and the PL lifetime of BTAA-Et in ethanol solution.

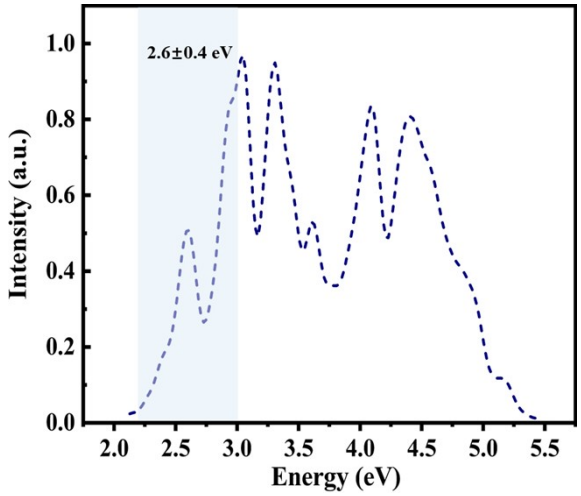

Figure S13. Simulated photoabsorption cross-section of BTAA-Et and the energy window of initial condition generation for excited-state dynamics simulations.

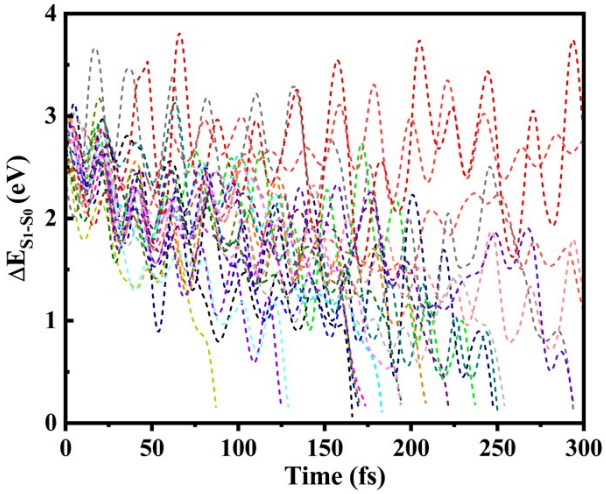

Figure S14. Time evolution of the S_1-S_0 energy differences in all simulation trajectories.

Table S2. Summary of the simulation results on the final step for BTAA-Et.

Traj. No.	Time-taken (fs)	E_{S1-S0} (eV)	*f*
1	166.0	0.065	0.0004
2	173.5	0.172	0.0006
3	237.0	0.185	0.0045
4	169.5	0.158	0.0046
5	183.0	0.114	0.0007
6	300.0	1.082	0.0366
7	87.0	0.158	0.0023
8	170.0	0.200	0.0076
9	247.5	0.140	0.0001
10	300.0	2.769	0.6146
11	294.0	0.088	0.0008
12	195.0	0.176	0.0001
13	250.0	0.115	0.0005
14	208.5	0.199	0.0001
15	300.0	1.258	0.0297
16	125.0	0.144	0.0005
17	221.5	0.174	0.0002
18	254.0	0.178	0.0023
19	300.0	2.764	0.0516
20	294.0	0.175	0.0006
21	129.0	0.160	0.0051
22	194.0	0.180	0.0007

Table S3. Cartesian coordinates of the averaged structure of the initial Franck-Condon (FC) structures form the excited-state dynamics simulations for BTAA-Et.

C	-0.21073103	4.46889369	-1.31224090
C	-0.01214178	5.58501317	-0.49495520
C	0.55823607	5.45633824	0.84218453
C	0.96323387	4.20324630	1.33283147
C	0.74656239	3.08093558	0.49505000
C	0.21896077	3.21834644	-0.82532430
N	1.04486035	1.78450705	0.87303528
C	0.79127195	0.96020024	-0.10119464
S	0.14116153	1.68055625	-1.59940813
C	1.04783868	-0.51018397	-0.05952708
C	2.44518080	-0.90277330	0.00745765
S	2.89698826	-2.62359346	0.13425042
C	4.56738907	-2.15350832	0.20406600
C	4.64457764	-0.70558586	0.17084340
N	3.46202530	-0.06914955	0.06871349
C	5.71489417	-2.90773099	0.28978197
C	6.93187762	-2.25849335	0.37990797

C	7.02630374	-0.86612431	0.36124669
C	5.91099783	-0.07184906	0.24290693
N	0.15621455	-1.44452853	-0.10846853
C	-1.20792137	-1.25789814	-0.07622923
C	-1.96468215	-2.24422183	-0.73330936
C	-3.35422418	-2.15750440	-0.78269762
C	-4.05143367	-1.07941697	-0.17061099
C	-3.26125050	-0.12972691	0.54660462
C	-1.89380667	-0.20964973	0.55794661
N	-5.42219310	-0.97782692	-0.25099886
C	-6.14935017	0.02447299	0.51084396
C	-6.19090628	-1.99741869	-0.98647222
C	-6.29309846	-0.30082888	2.03845466
C	-6.49327961	-3.27936509	-0.19128476
H	-0.63319124	4.60632560	-2.33143831
H	-0.33764773	6.57622890	-0.86573365
H	0.74728265	6.31772017	1.51004499
H	1.46000260	4.09684776	2.34174112
H	5.67338210	-4.00152974	0.35719785
H	7.86631140	-2.86102777	0.43751539
H	8.02795832	-0.38298238	0.43874233
H	5.97021925	0.98115817	0.30119557
H	-1.44458639	-3.04842481	-1.23690481
H	-3.86532134	-2.94676089	-1.27620137
H	-3.73940216	0.62337308	1.10338657
H	-1.33139922	0.53133939	1.11396742
H	-7.18139283	0.12485065	0.06785802
H	-5.66175013	1.01403066	0.40086891
H	-5.69869004	-2.21857787	-1.90723603
H	-7.14577390	-1.53295170	-1.33481049
H	-6.86410365	0.52794978	2.49034478
H	-6.80795949	-1.27926252	2.21642839
H	-5.30867100	-0.37468740	2.53310578
H	-6.98671193	-4.02538202	-0.82677591
H	-5.55397184	-3.72069552	0.18794367
H	-7.12193500	-3.05115661	0.67213123

Table S4. Cartesian coordinates of the averaged structure of the final Conical intersection (CI) structures from the excited-state dynamics simulations for BTAA-Et.

C	-0.39666019	4.55280480	-1.40066623
C	-0.28999599	5.67965648	-0.62508140
C	0.30827917	5.58178259	0.64249305
C	0.82568892	4.39501636	1.09617937
C	0.71820138	3.28930750	0.28181461

C	0.13008480	3.39106362	-0.96564485
N	1.19633587	2.04000470	0.64607597
C	0.98671333	1.19059491	-0.30912578
S	0.13643559	1.81841705	-1.73063028
C	1.15044247	-0.26290172	-0.20615350
C	2.43052945	-0.77968927	0.21300871
S	2.76070411	-2.51201227	0.24578722
C	4.42951638	-2.21271993	0.41624468
C	4.61735609	-0.84897766	0.43776268
N	3.47942958	-0.11721021	0.31338498
C	5.52693072	-3.09963049	0.46370332
C	6.77349563	-2.57430222	0.51967430
C	6.94891482	-1.23176253	0.53176488
C	5.89389970	-0.37799410	0.45597629
N	0.15522573	-0.96425368	-0.82371858
C	-1.05224590	-1.34055247	-0.42946266
C	-1.98393121	-1.70213095	-1.40579961
C	-3.33658883	-1.72330442	-1.21167431
C	-3.89898432	-1.33403440	-0.01668003
C	-2.98824733	-1.08860702	1.02754762
C	-1.62615329	-1.14909930	0.82772090
N	-5.24734042	-1.13844190	0.17913775
C	-5.76952911	-0.16859276	1.04032055
C	-6.17069802	-1.73602908	-0.70380381
C	-6.53772731	-0.59789181	2.18997218
C	-6.42039828	-3.07416872	-0.40221306
H	-0.84924628	4.60112301	-2.35982606
H	-0.57857982	6.63652969	-1.00302792
H	0.41782584	6.48414106	1.21512338
H	1.27624638	4.32305085	2.01547542
H	5.33081112	-4.15757701	0.51271992
H	7.61177626	-3.20887253	0.54831573
H	7.92306314	-0.89722174	0.64670195
H	6.01262838	0.63308212	0.44372374
H	-1.51929221	-1.95735919	-2.28250163
H	-3.91915212	-1.95318192	-2.02352833
H	-3.40196581	-0.86751481	1.97167235
H	-1.00169974	-0.90415586	1.62915091
H	-6.38294475	0.42979698	0.49114995
H	-5.02319214	0.48734157	1.28124463
H	-5.82999445	-1.61628548	-1.62297041
H	-7.04932586	-1.26469900	-0.62756110
H	-6.80935346	0.17027698	2.78921666
H	-7.35526109	-1.06964076	1.93438230

H	-5.97012481	-1.20625162	2.72388746
H	-7.06941042	-3.60368633	-0.96216062
H	-5.58703761	-3.57022935	-0.38881955
H	-6.79038584	-3.14240958	0.51161508

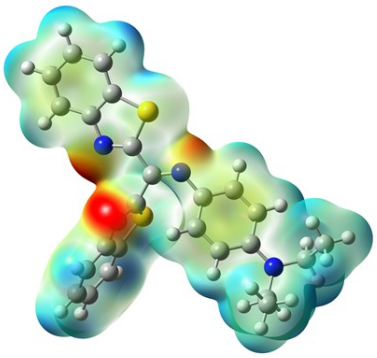

Figure S15. Electrostatic potential (ESP) map of BTAA-Et. The red denotes electron-rich regions, and the blue represents electron-poor sites.

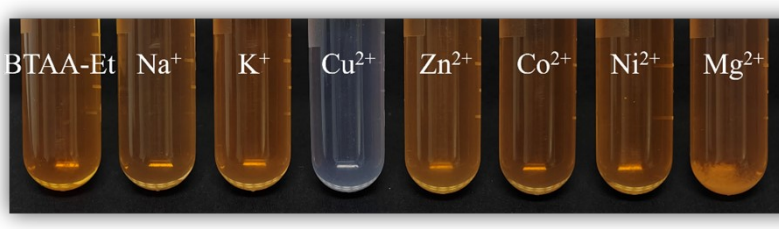

Figure S16. Color change of BTAA-Et solution upon the addition of various metal ions.

Table S5. Detailed molar ratios of BTAA-Et and Cu^{2+} for Job's plot assessment.

Cu^{2+} (μmol)	BTAA-Et (μmol)	Ratio of Cu^{2+}
0.5	4.5	10%
1.0	4.0	20%
1.5	3.5	30%
2.0	3.0	40%
2.5	2.5	50%
3.0	2.0	60%
3.5	1.5	70%
4.0	1.0	80%
4.5	0.5	90%

Figure S17. Color change of BTAA-Et ethanol solutions after adding varying equivalents of Cu^{2+} (0.0–1.0 eq).

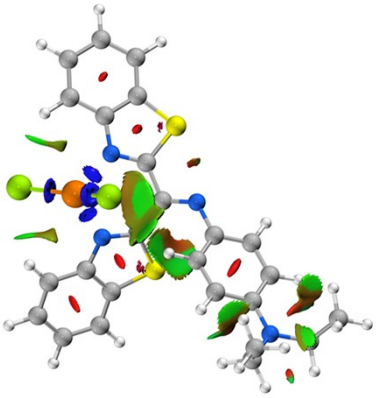

Figure S18. Inter/intramolecular interactions in the complex of BTAA-Et with $CuCl_2$. The red and blue represent strong repulsive and attractive forces, respectively, while the green shows weak van der Waals (vdW) interactions.

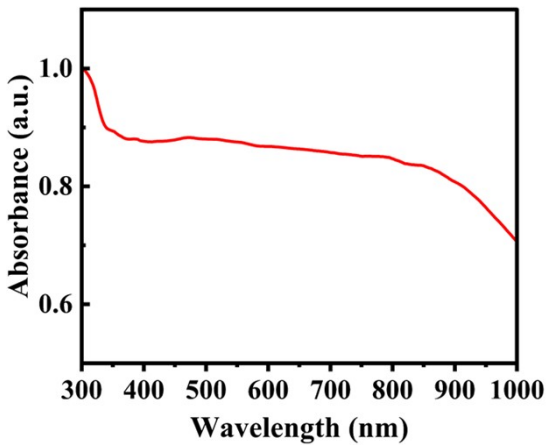

Figure S19. UV-Vis-NIR absorption spectrum of Cu^{2+}@BTAA-Et solids.

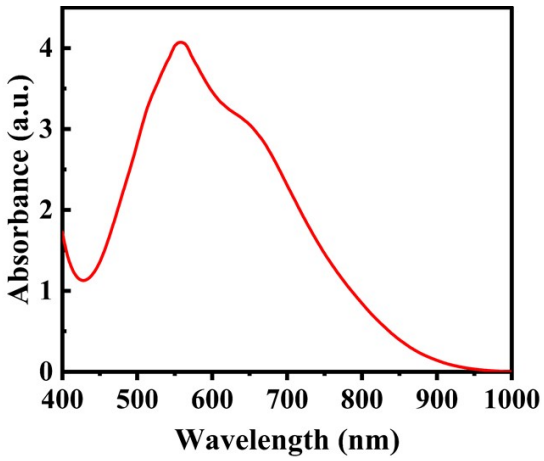

Figure S20. Absorption spectrum of Cu^{2+}@BTAA-Et in ethanol solution (200 μmol).

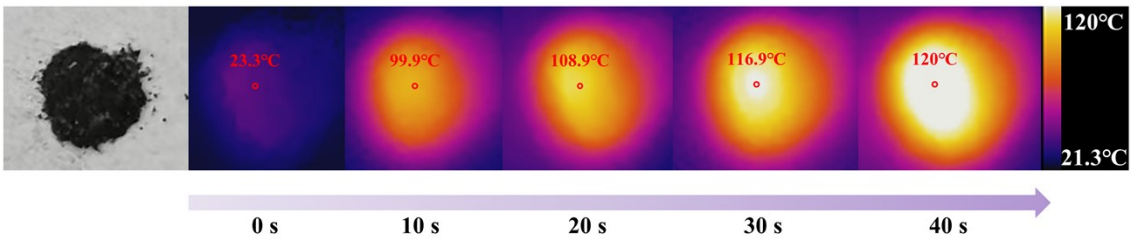

Figure S21. Infrared images of Cu^{2+}@BTAA-Et solids during the photothermal heating process under 808 nm laser irradiation (0.2 W·cm^{-2}).

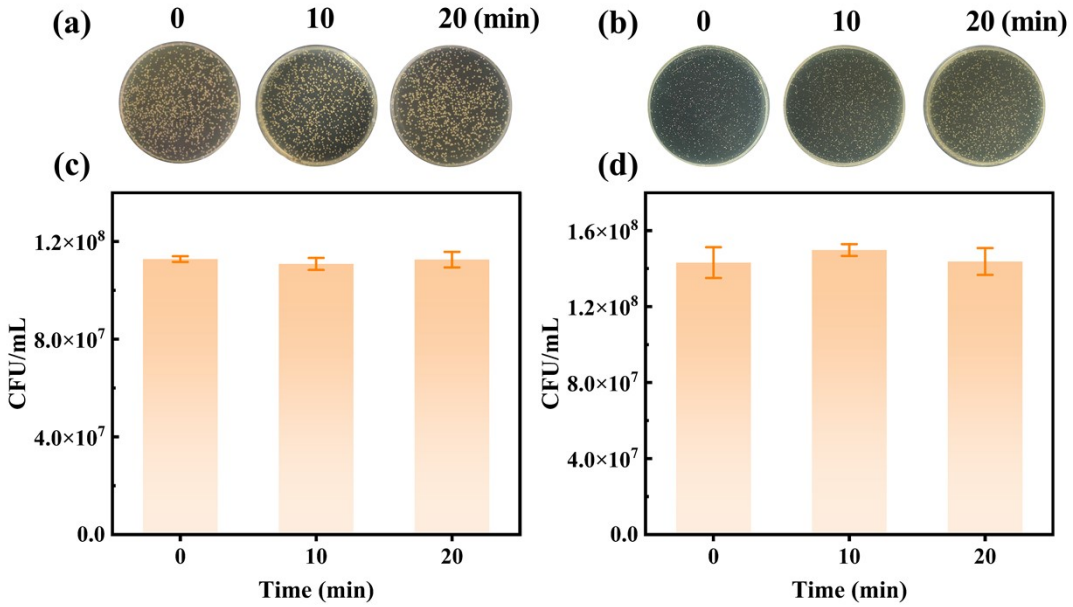

Figure S22. Antibacterial performance of Cu^{2+}@BTAA-Et after incubating with bacteria for different times (0, 10, and 20 min) in dark environments. Colony images of *S. aureus*(a) and *E. coli* (b), and the counting statistics for *S. aureus*(c) and *E. coli* (d), respectively.

Table S6. Comparison of PTCEs of representative organic-metal materials reported recently in the literature.

Paper Title	Materials Name	PTCE	Laser	Year of Publication
GSH/pH dual-activated POM@MOF for tumor cell-specific synergistic photothermal and chemodynamic therapy[5]	PMo_{12}@MIL-101	47.0 %	808 nm	2024
Dual functionality of phosphorescence and photothermal conversion through light-activated open-shell singlet diradicals in silver metal–organic frameworks[6]	Ag-MOF 1	49.1 %	808 nm	2025
Construction of Rough Surfaces Based on Zirconium Metal-Organic Frameworks to Enhance Photothermal and Photodynamic Therapy for Multiple Myeloma[7]	UiO@CeO_2/IR@(bPEI/HA)-A6	26.8 %	NIR	2026
An intelligent NIR-IIb-responsive lanthanide@metal-organic framework core-shell nanocatalyst for combined deep-tumor therapy[8]	UCNPs@ZrMOF@ICG	28%	808 nm	2024
A RuII Polypyridyl Alkyne Complex Based Metal–Organic Frameworks for Combined Photodynamic/Photothermal /Chemotherapy[9]	UiO-Ra-DOX-CuS	26.8 %	NIR	2019
Tuning Donor–Acceptor Stacking in MOFs via Rational Metal Coordination for Enhanced Photothermal Conversion and Solar-Driven Water Evaporation Performance[10]	TTFDPNI-Cd-MOF and TTFDPNI-Co-MOF	47.5 % and 39.4 %	808 nm	2025
Rigid coordination environment induced MOFs	TTFBDAT	28.9	808	2024

Paper Title	Materials Name	PTCE	Laser	Year of Publication
to achieve an efficient photothermal conversion efficiency[11]	-Zn-MOF	%	nm	
Stable Nickel-Based Metal–Organic Framework Containing Thiophene/Diimidazole Units for Effective Near-Infrared Photothermal Conversion[12]	L1	10.8 %	660 nm	2022
Band gap modulation enabled by TCNQ loading in a Ru-based metal–organic framework for enhanced near-infrared absorption and photothermal conversion[13]	TCNQ@Ru-MOF	29.1 %	980 nm	2021
A Mn-incorporated porphyrinic metal-organic framework with near-infrared light responsive photothermal effect and intrinsic ROS scavenging ability for promoted healing of bacteria-infected wounds[14]	Mn@PCN-224	34.1 %	NIR	2026
Photoresponsive MXene/HKUST-1@CuS antimicrobial nanosheets towards efficient solar-driven water evaporation and biofilm eradication[15]	MX/HK@CuS	38%	808 nm	2026
Rational design of iridium–porphyrin conjugates for novel synergistic photodynamic and photothermal therapy anticancer agents[16]	4-Ir NPs	49.5 %	635 nm	2021
Structural optimization of organometallic cages for enhanced photothermal solar water evaporation[17]	Cages 1-4	30.0~35.0 %	730 nm	2025

Paper Title	Materials Name	PTCE	Laser	Year of Publication
π-d Conjugated Coordination Nanoparticles Engineered by CuNi-MOF: A Rationally Designed NIR-II Photothermal Platform for Biosensing[18]	$Ni(DMPD^{ISQ})_2$	42.7 %	1064 nm	2025
Self-Assembled Aza-BODIPY and Iron(III) Nanoparticles for Photothermal-Enhanced Chemodynamic Therapy in the NIR-II Window[19]	ABFe NPs	55%	1064 nm	2023

Table S7. Inhibition of *E. coli* and *S. aureus* by Cu^{2+}@BTAA-Et with different concentrations. Bacteria were treated with indicated concentrations, incubated at 37°C for 16 h (with/without 808 nm laser irradiation, 1.0 W/cm², 20 min), and the growth was assessed by measuring the OD_{600}.

Cu^{2+}@BTAA-Et concentration (μM)	OD_{600} for *S. aureus*		OD_{600} for *E. coli*	
	Dark	NIR_{808nm}	Dark	NIR_{808nm}
0	0.88 ± 0.06	0.86 ± 0.05	0.89 ± 0.03	0.87 ± 0.04
4	0.85 ± 0.02	0.80 ± 0.03	0.87 ± 0.05	0.82 ± 0.02
8	0.81 ± 0.06	0.68 ± 0.05	0.84 ± 0.07	0.71 ± 0.05
16	0.77 ± 0.04	0.55 ± 0.04	0.75 ± 0.05	0.59 ± 0.04
32	0.65 ± 0.02	0.37 ± 0.03	0.61 ± 0.04	0.44± 0.03
64	0.56 ± 0.04	0.21 ± 0.02	0.49 ± 0.03	0.29 ± 0.02
128	0.31 ± 0.03	0.05 ± 0.01	0.29 ± 0.02	0.04 ± 0.01
256	0.13 ± 0.02	0.02 ± 0.01	0.10 ± 0.03	0.03 ± 0.01
512	0.08 ± 0.01	—	0.06 ± 0.01	—

Table S8. Minimum inhibitory concentration (MIC) of Cu^{2+}@BTAA-Et against *S. aureus* and *E. coli*. The MIC values were determined as the lowest concentration of the complex that results in the complete inhibition (OD_{600} < 0.1) of visible bacterial growth.

Bacteria	Condition	MIC (μM)
S. aureus	Dark	512
S. aureus	NIR_{808nm}	128
E. coli	Dark	512
E. coli	NIR_{808nm}	128

Supplementary references

1. Yan-Zhao Liu, Xiao-Yun Ran, Ding-Heng Zhou, et al., Novel Dibenzofulvene-Based NIR-II Emission Phototheranostic Agent with an 82.6% Photothermal Conversion Efficiency for Photothermal Therapy. *Adv. Funct. Mater.*, 2023;34(8):2311365.
2. Peirong Bai, Qiong Zhang, Xiaoyu Zhang, et al., NIR-Absorbing Organic Charge Transfer Complexes for Photothermal Antibacterial Therapy and Wounds Healing. *Mater. Today Bio*, 2025;35:102411.
3. Jiangrong Li, Qiuyang Zhang, Zhiwei Chen, et al., Postsynthetic Modification of Thermo-Treated Metal–Organic Framework for Combined Photothermal/Photodynamic Antibacterial Therapy. *ACS Appl. Mater. Interfaces*, 2024;16(7):8459-8473.
4. Xiaoliang Qi, Yajing Xiang, Erya Cai, et al., Inorganic–organic hybrid nanomaterials for photothermal antibacterial therapy. *Coord. Chem. Rev.*, 2023;496:215426.
5. Bole Li, Zhujun Wu, Xiaotong Xu, et al., GSH/pH dual-activated POM@MOF for tumor cell-specific synergistic photothermal and chemodynamic therapy. *Inorg. Chem. Front.*, 2024;11(14):4439-4448.
6. Pei-Yu Liao, Jia-Chuan Liu, Hao-Zhi Fan, et al., Dual functionality of phosphorescence and photothermal conversion through light-activated open-shell singlet diradicals in silver metal–organic frameworks. *J. Mater. Chem. C*, 2025;13(32):16712-16721.
7. Junghan Lee, Kwangsun Yu, Enkhzaya Davaa, et al., Autophagy-Regulating, Photothermal Polydopamine-Coated, and Photodynamic Zirconium/Porphyrin-Framed Metal–Organic Frameworks for Enhanced Doxorubicin Therapy in Colon Cancer. *Biomater. Res.*, 2025;29(0218).
8. Chaoqun Jiang, Yu Chen, Xiaolong Li, et al., An intelligent NIR-IIb-responsive lanthanide@metal–organic framework core–shell nanocatalyst for combined deep-tumor therapy. *J. Mater. Chem. B*, 2024;12(35):8626-8632.
9. Xiaochun Hu, Yonglin Lu, Chunyan Dong, et al., A RuII Polypyridyl Alkyne Complex Based Metal-Organic Frameworks for Combined Photodynamic/Photothermal/Chemotherapy. *Chem. Eur. J.*, 2019;26(7):1668-1675.
10. Xin-Yu Zheng, Cong Wang, Xu-Feng Luo, et al., Tuning Donor–Acceptor Stacking in MOFs via Rational Metal Coordination for Enhanced Photothermal Conversion and Solar-Driven Water

Evaporation Performance. *Inorg. Chem.*, 2024;1321(139959).
11. Xin-Yu Zheng, Liangjun Shen, Xu-Feng Luo, et al., Rigid coordination environment induced MOFs to achieve an efficient photothermal conversion efficiency. *J. Mol. Struct.*, 2024;1321(139959).
12. Xiangran Pei, Lilong Dang, Tingting Zhang, et al., Stable Nickel-Based Metal–Organic Framework Containing Thiophene/Diimidazole Units for Effective Near-Infrared Photothermal Conversion. *Catalysts*, 2022;12(7):777.
13. Tao Zhang, Jian-Wei Cao, Xue Jiang, et al., Band Gap Modulation Enabled by TCNQ Loading in a Ru-Based Metal–Organic Framework for Enhanced Near-Infrared Absorption and Photothermal Conversion. *Cryst. Growth Des.*, 2021;21(2):729-734.
14. Haihan Song, Mengli Zhang, Zhefeng Qian, et al., A Mn-incorporated porphyrinic metal-organic framework with near-infrared light responsive photothermal effect and intrinsic ROS scavenging ability for promoted healing of bacteria-infected wounds. *Colloids Surf. B Biointerfaces*, 2026:115460
15. Yingfeng Wang, Ming Huang, Maoli Yin, et al., Photoresponsive MXene/HKUST-1@CuS antimicrobial nanosheets towards efficient solar-driven water evaporation and biofilm eradication. *J. Environ. Chem. Eng.*, 2026:121313.
16. Liping Zhang, Yun Geng, Lijuan Li, et al., Rational design of iridium–porphyrin conjugates for novel synergistic photodynamic and photothermal therapy anticancer agents. *Chem. Sci.*, 2021;12(16):5918-5925.
17. Xiao-Qian Wan, Ya-Ning Xu, Jian-Xin Yang, et al., Structural optimization of organometallic cages for enhanced photothermal solar water evaporation. *Chin. J. Struct. Chem.*, 2025:100705.
18. Jinju Xu, Xingying Wang, Tian Lan, et al., π-d Conjugated Coordination Nanoparticles Engineered by CuNi-MOF: A Rationally Designed NIR-II Photothermal Platform for Biosensing. *Anal. Chem.*, 2025;97(49):27427-27435.
19. Jinjin Zhang, Yaojun Li, Minling Jiang, et al., Self-Assembled Aza-BODIPY and Iron(III) Nanoparticles for Photothermal-Enhanced Chemodynamic Therapy in the NIR-II Window. *ACS Biomater. Sci. Eng.*, 2023;9(2):821-830.